

Gravitational Lensing of Core Collapse Supernova Gravitational Wave Signals

RAHUL RAMESH, ASHISH KUMAR MEENA and JASJEET SINGH BAGLA*.

Department of Physical Sciences, IISER Mohali, Sector 81, SAS Nagar, Punjab, India - 140306.

*Corresponding author. E-mail: jasjeet@iisermohali.ac.in

MS received xx yy 2021; accepted xx yy 2021

Abstract. We discuss the prospects of gravitational lensing of gravitational waves (GWs) coming from core-collapse supernovae (CCSN). As the CCSN GW signal can only be detected from within our own Galaxy and the local group by current and upcoming ground-based GW detectors, we focus on microlensing. We introduce a new technique based on analysis of the power spectrum and association of peaks of the power spectrum with the peaks of the amplification factor to identify lensed signals. We validate our method by applying it on the CCSN-like mock signals lensed by a point mass lens. We find that the lensed and unlensed signal can be differentiated using the association of peaks by more than one sigma for lens masses $M_L > 150M_\odot$. We also study the correlation integral between the power spectra and corresponding amplification factor. This statistical approach is able to differentiate between unlensed and lensed signals for lenses as small as $M_L \sim 15M_\odot$. Further, we demonstrate that this method can be used to estimate the mass of a lens in case the signal is lensed. The power spectrum based analysis is general and can be applied to any broad band signal and is especially useful for incoherent signals.

Keywords. Gravitational lensing: micro; gravitational waves

1. Introduction

The detection of gravitational waves (GWs) from merging binaries by Laser Interferometer Gravitational-wave Observatory (LIGO) and Virgo (Abbott *et al.*, 2019, 2020) marked the beginning of a new field to study the Universe. With improvements in sensitivity of existing detectors and upcoming facilities like the Kamioka Gravitational Wave Detector (KAGRA, Somiya, 2012), and LIGO-India (Unnikrishnan, 2013), the number of such GW sources will continuously increase.

In addition to chirp signals emitted by merging binaries, core-collapse supernovae (CCSN) also emit GWs in LIGO/Virgo frequency range (10 Hz – 10^4 Hz) (Ott, 2009; Fryer & New, 2011). Detailed multi-dimensional CCSN simulations and other studies (e.g., Ott *et al.*, 2013; Kuroda *et al.*, 2014; Radice *et al.*, 2019; Sotani *et al.*, 2021) indicate that the corresponding GW signals are around ~ 1 second long and can only be detected up to a distance of 100 kpc with the existing and upcoming advanced network of ground-based detectors. This distance covers our galaxy and the nearby Magellanic Clouds, which leads to an event rate of ~ 2 CCSN/100 yr. However, some extreme models also suggest the possibility of GW signal detection

from a distance of ~ 100 Mpc by the advanced ground-based network with an event rate of ~ 2 CCSN/yr (e.g., Fryer *et al.*, 2002; Ott *et al.*, 2006; Piro & Pfahl, 2007). However, these are already constrained by a lack of observations of such events in the last few years.

As discussed (extensively) in literature, GW signals are also subject to gravitational lensing similar to electromagnetic radiation (e.g., Broadhurst *et al.*, 2018; Haris *et al.*, 2018; Li *et al.*, 2018; Xu *et al.*, 2021). However, due to the large wavelength of GWs in the LIGO/Virgo frequency range, microlensing can introduce frequency-dependent effects in the GW signal (e.g., Christian *et al.*, 2018; Diego *et al.*, 2019; Meena & Bagla, 2020; Mishra *et al.*, 2021). Currently, LIGO/Virgo can detect GWs emitted by merging binaries out to cosmological distances. Hence, one can look for the signature of both strong lensing and microlensing in these signals. However, as mentioned above, due to an order of magnitude weaker GW signal in CCSN, one can only detect them from within the local group. Hence, only galactic microlenses can introduce the lensing effect in CCSN GW signals.

In our current work, we look at the prospects of observing galactic microlensing signatures in the CCSN GW signals. We also discuss possible methods based on the power spectrum analysis of the GW signal that

can be used to find lensed signals. We validate our methodology using CCSN-like mock GW signals generated using the Gaussian random fields. Although this method is able to differentiate between lensed and unlensed GW signals, it is not effective for all lens masses. Hence, we also discuss the possible limitations of our method.

This paper is organized as follows: In §2., we review the relevant basics of gravitational lensing. In §3., we consider mock waveforms as model signals to give an overview of the various features that are expected when signals are lensed in the regime where wave effects are non negligible. In §4., we describe the procedure that we have used to generate CCSN-like GW signals. We present results in §5.. In §5.1, we discuss the effect of lensing on the the CCSN-like GW signal and the corresponding power spectrum. The methods to identify lensed signals are discussed in §5.2. In §5.3, we discuss a possible application of the correlation integral in the estimation of (point mass) lens parameters. Limitations of these methods are discussed in §5.4. Conclusion and summary are presented in §6..

2. Basics of Gravitational Lensing

For cases where the wavelength of the signal coming from a source is very small compared to the Schwarzschild radius of the lens ($\lambda \ll R_{\text{Sch}}$), one can use the conventional geometric optics to study the gravitational lensing (Schneider *et al.*, 1992). However, if the signal wavelength is of the order of the Schwarzschild radius of the lens ($\lambda \sim R_{\text{Sch}}$) then wave effects become non-negligible (Nakamura & Deguchi, 1999; Takahashi & Nakamura, 2003). In such cases, the amplification factor is given as:

$$F(f, \mathbf{y}) = \frac{\xi_0^2}{c} \frac{D_s(1+z_d)}{D_d D_{ds}} \frac{f}{i} \int d^2\mathbf{x} \exp[2\pi i f t_d(\mathbf{x}, \mathbf{y})], \quad (1)$$

where f is the frequency of the signal and z_d is the lens redshift. D_d , D_s , and D_{ds} are the angular diameter distances from observer to lens, observer to source, and from lens to source, respectively. $\mathbf{y} = \boldsymbol{\eta} D_d / \xi_0 D_s$ and $\mathbf{x} = \boldsymbol{\xi} / \xi_0$ are the dimensionless source and image position in the source and image plane, respectively. Here ξ_0 is an arbitrary length scale to make the equation dimensionless. The time-delay factor, t_d , between lensed and unlensed images is given as:

$$t_d = \frac{\xi_0^2}{c} \frac{D_s}{D_d D_{ds}} (1+z_d) \left[\frac{(\mathbf{x}-\mathbf{y})^2}{2} - \psi(\mathbf{x}) + \phi_m(\mathbf{y}) \right], \quad (2)$$

where $\psi(\mathbf{x})$ is the lens potential and $\phi_m(\mathbf{y})$ is a constant which can be chosen to simplify the calculations. In our present work, we choose $\phi_m(\mathbf{y})$ such that the time delay corresponding to the global minimum is zero.

One cannot solve Equation 1 analytically for complex lens mass models. Only the isolated point mass lens (of mass M_L) has an analytic solution which is given as (Peters, 1974):

$$F(\omega, \mathbf{y}) = \exp \left[\frac{\pi\omega}{4} + \frac{i\omega}{2} \left\{ \ln \left(\frac{\omega}{2} \right) - 2\phi_m(x_m) \right\} \right] \Gamma \left(1 - \frac{i\omega}{2} \right) {}_1F_1 \left(\frac{i\omega}{2}, 1; \frac{i\omega}{2} y^2 \right), \quad (3)$$

where

$$\omega = \frac{8\pi G M_L (1+z_d) f}{c^3}; \quad \phi_m(\mathbf{y}) = \frac{(x_m - y)^2}{2} - \ln x_m, \quad (4)$$

with $x_m = (y + \sqrt{y^2 + 4})/2$. Here, Einstein radius of the point mass lens is used as the length scale. In case of geometric optics limit, $\lambda \ll R_{\text{Sch}}$, Equation 3 can be written as

$$F(f, \mathbf{y}) = \sqrt{\mu_+} - \iota \sqrt{\mu_-} \exp[2\pi i f \Delta t_d], \quad (5)$$

where μ_{\pm} denote the amplification factor for primary and secondary image for a point mass lens in geometric optics limit and Δt_d is the time delay between these two images. In reality, stellar mass microlenses are extended objects. Hence, one needs to verify that the point mass lens approximation is valid for microlenses. We validate this approximation in Appendix A., and consider microlenses as point masses throughout this work.

From Equation 3, for a given frequency value, one can see that lensing due to a point mass lens depends only on the lens mass and the source position. Figure 1 represents the dependency of amplification factor on these two parameters. In the top row, the lens mass is fixed at $100M_{\odot}$ and the source position is varied. One can see that, as the source moves towards the center, the amplitude of oscillations in both amplification factor ($|F|$; left panel) and phase shift (θ_F ; right panel) increases. However, the frequency of these oscillations decreases. Apart from that, the first peak in the amplification factor ($|F|$) also moves towards the high frequencies. On the other hand, the lower row represents the variation in the lens mass for a fixed source position ($y = 1$). One can see that fixing the source position determines the amplitude of the oscillations in both the amplification factor ($|F|$) and the phase shift (θ_F). An increase in the lens mass increases the frequency of the oscillations starting from the lower frequency values.

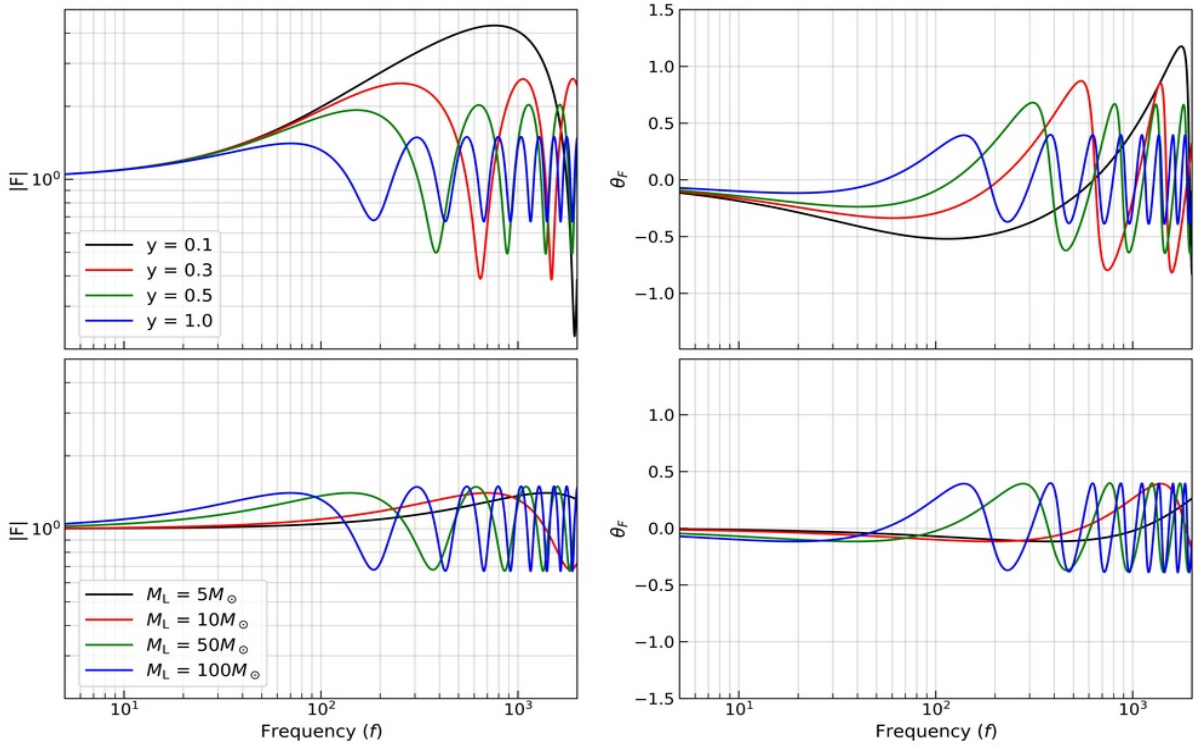


Figure 1. Gravitational lensing due to a point mass lens: The top row represents the amplification factor ($|F|$) and phase shift (θ_F) as a function of frequency due to a point mass lens of $100M_\odot$ with different source positions (y) in left and right panel, respectively. The lens redshift has been set to zero (i.e., $z_L = 0$). Similarly, the bottom row shows the amplification factor and phase shift factor due to a point lens with different lens mass values with the source position fixed at $y = 1$.

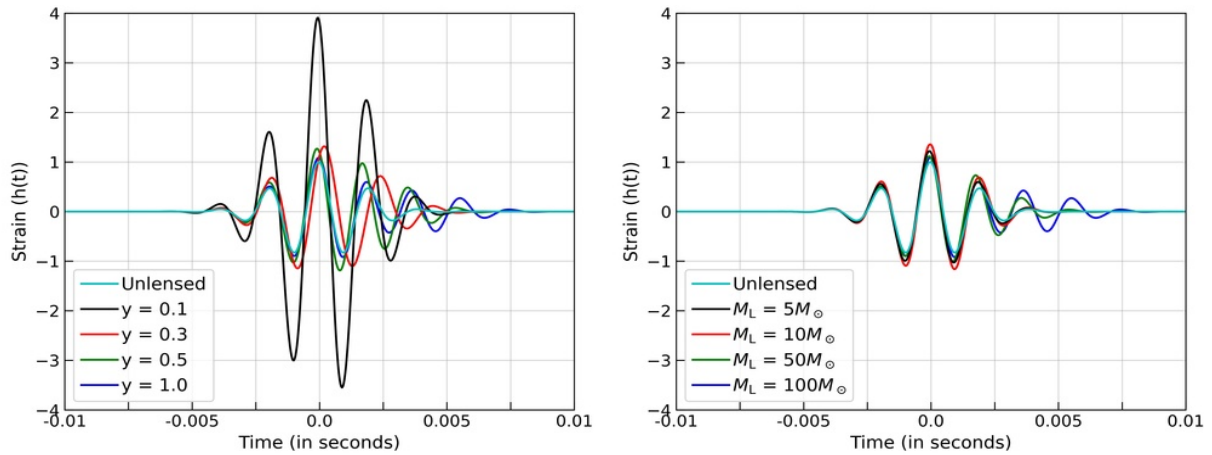


Figure 2. Lensing of a Gaussian wave packet due to a point mass lens: The left panel represents the unlensed (cyan) and lensed Gaussian wave packet with a lens mass of $100M_\odot$ and different source positions (y). The y -values for different lensed curves are shown in the legend. Similarly, the right panel represents the unlensed (cyan) and lensed Gaussian wave packets with different lens mass values and fixed source position ($y = 1$). In both panels, the x-axis represents the time and y-axis represents the normalized strain of the GW signal. As the source position and lens mass values are same as the Figure 1, one can clearly see the same trend in both figures.

Throughout this paper, unless otherwise mentioned, we always fix the source at $y = 1$.

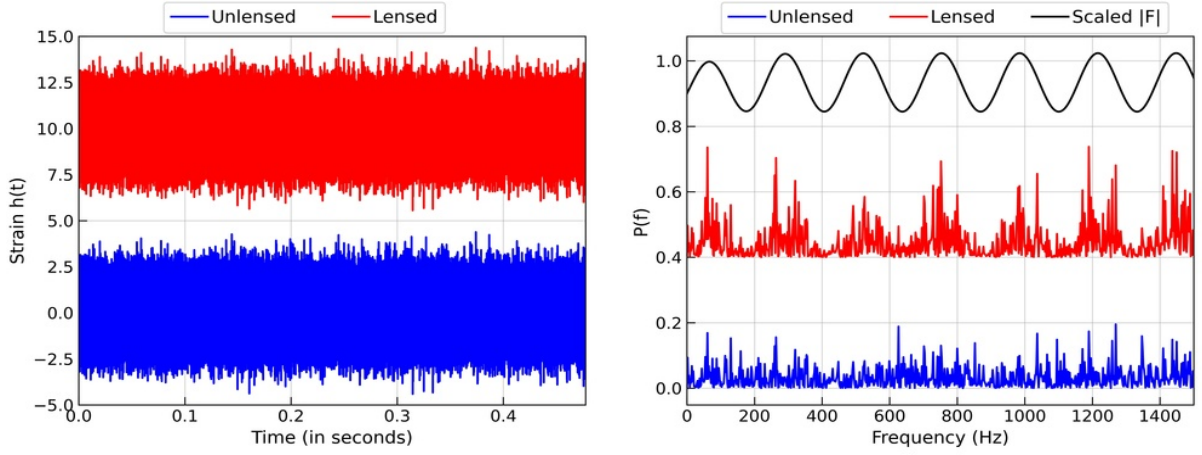


Figure 3. Lensing of white noise due to a point mass lens: The left panel shows the unlensed (blue) and lensed (red) signals. We here consider $M_L = 100M_\odot$. The two signals have been vertically displaced for better visibility. As can be seen, it is almost impossible to differentiate between the two signals, owing to the fact that white noise shows no particular evolution of frequency with time. The right panel shows the corresponding power spectra, in corresponding colors. Again, the two curves have been vertically displaced. For reference, we also show (a scaled version of) the modulus of the amplification factor. The power of the lensed signal oscillates in accordance with the oscillations of the amplification factor, while the power spectrum of the unlensed signal shows stochastic oscillations.

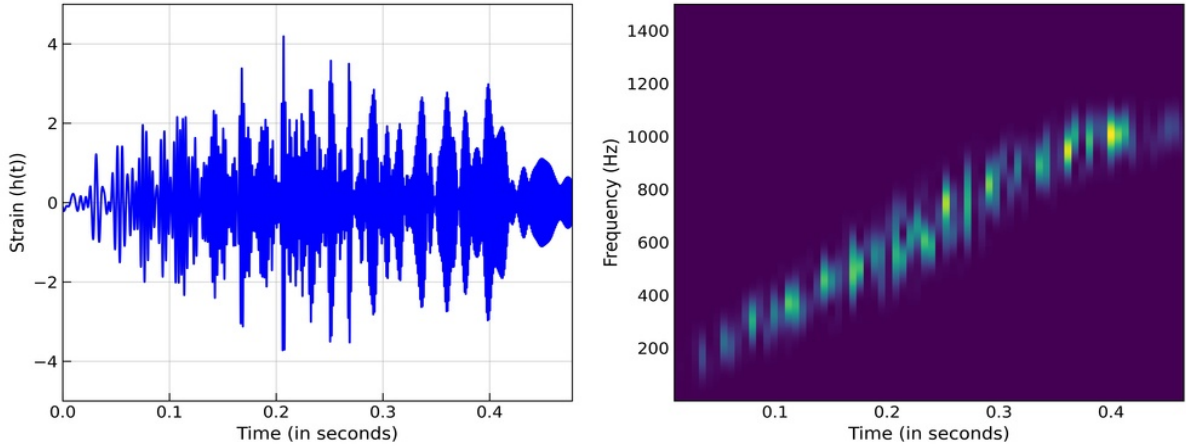


Figure 4. Simulated CCSN-like GW signal: The left panel represents the CCSN-like GW signal generated by the method described in §4. The x-axis represents the time and y-axis represents the normalized strain. The right panel represents the corresponding frequency-time spectrogram. The x-axis represents the time and the y-axis represent the frequency values.

3. Lensing of Ideal Gravitational Wave Signals

Unlike chirp signals emitted from a merging binary, CCSN events give rise to broadband incoherent GW signals with a duration of ~ 1 second in the time domain. Due to its simplicity and broadband nature, a Gaussian wave packet is an obvious starting point to gain initial insights about the lensing of CCSN GW signals. The Gaussian wave packet (in time domain) is given as

$$h(t) = \exp\left[-2\pi^2\sigma^2(t-t_0)^2\right]\exp(2\pi if_0t), \quad (1)$$

where f_0 and σ are the central frequency and standard deviation of the wave packet (in frequency domain). Figure 2 shows the lensing effect due to a point mass lens on a Gaussian wave packet with a central frequency of 500 Hz and a standard deviation of 100 Hz. In both panels, the x-axis represents the time, and the y-axis shows the signal amplitude. Similar to Figure 1, the left panel of the source position has been varied while fixing the lens mass to $100M_\odot$, whereas in the right panel, the lens mass is varied while keeping the source at $y = 1$. In the right panel, one can see that both lensed and unlensed signals arrive at the same

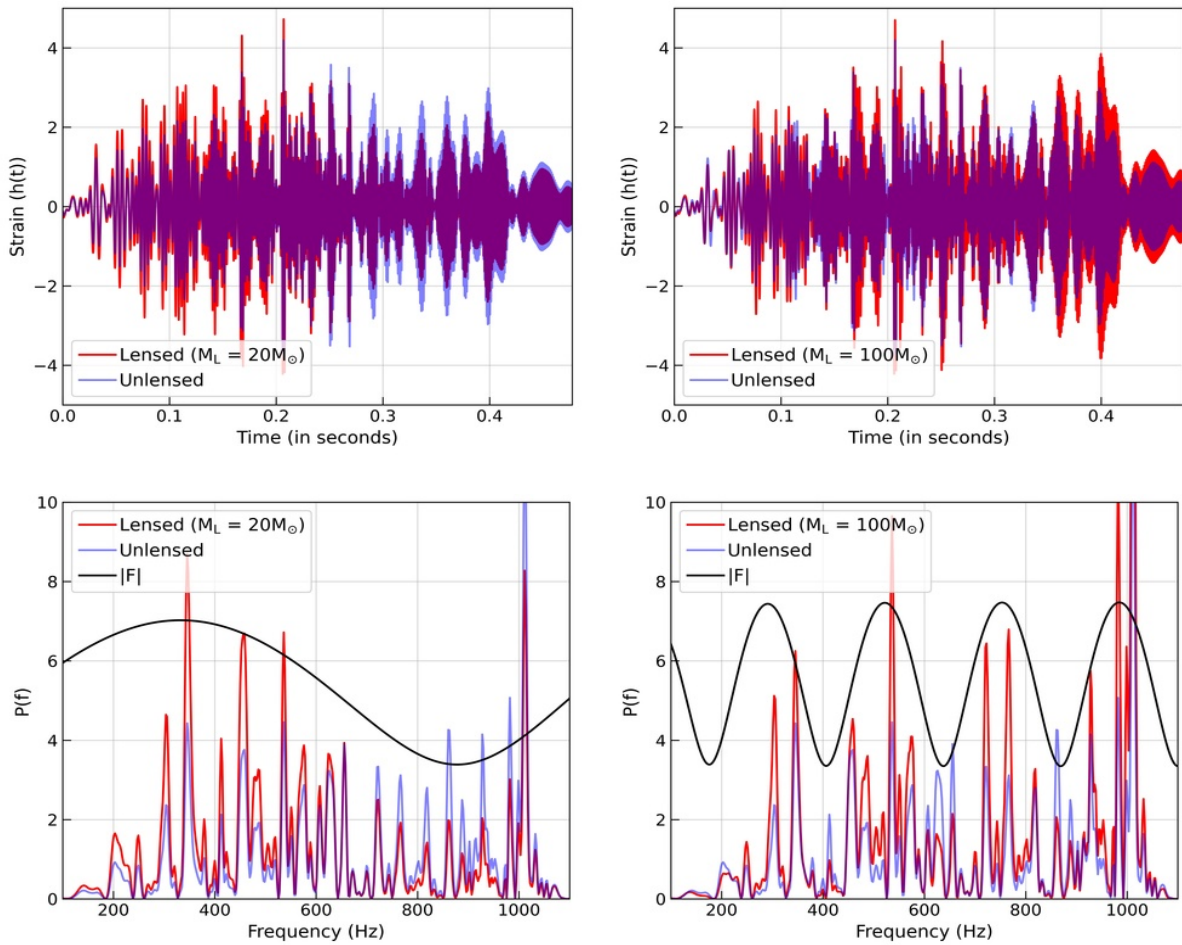


Figure 5. Lensed CCSN-like GW signal and the corresponding Power spectrum corresponding to Figure 4: The top left panel represents the lensed (unlensed) signal in red (blue) with the lens mass $20M_{\odot}$. The top right panel represents the same signal lensed with a lens mass of $100M_{\odot}$. The bottom left panel represents the power spectrum ($P(f)$) of lensed (by a $20M_{\odot}$) and unlensed signal in red and blue, respectively. The black solid line represents the amplification factor ($|F|$) due to lens mass. The amplification factor is scaled by a factor of five to (i.e., $5|F|$) to separate it from the power spectrum. The right panel is a similar plot for the lens mass of $100M_{\odot}$.

time as we set the time delay for the minima image to zero. However, the lensed signal is not only amplified but also has a spread in time larger than the unlensed signal. It can be understood from the right panel of the figure: one can see that as we increase the lens mass, the duration of the signal increases. This is because the lensed signal represents the interference between the minima and saddle images which forms in the geometric optics regime. As we increase the lens mass, the time delay between these two image increases, so the final signal has a longer duration as the saddle image part gets delayed as compared to the minima. It becomes clearer if we increase the lens mass (or move the source away from the center), which increases the time delay between the two images. Eventually, the time delay between the two images exceeds the duration of the signal, and we observe two separate signals. Equivalent

to the above description, one can also think of lensing in terms of oscillations of the amplification factor: as the amplification factor oscillates faster (corresponding to a greater time delay), a greater distortion is observed in the signal.

To illustrate some key aspects using a simple example, we consider white noise as a test signal. This is broad band and incoherent. By definition, such a signal has no frequency structure or evolution of the power spectrum over time, unlike the expected signal from CCSN. As a result, unlike the Gaussian wave packet example, it is not straightforward to identify differences between the lensed and unlensed waveforms. The left panel of Figure 3 shows an example of lensed (red) and unlensed (blue) versions of white noise. We here take $M_L = 100M_{\odot}$. The lensed signal is shifted vertically for a better comparison between lensed and unlensed

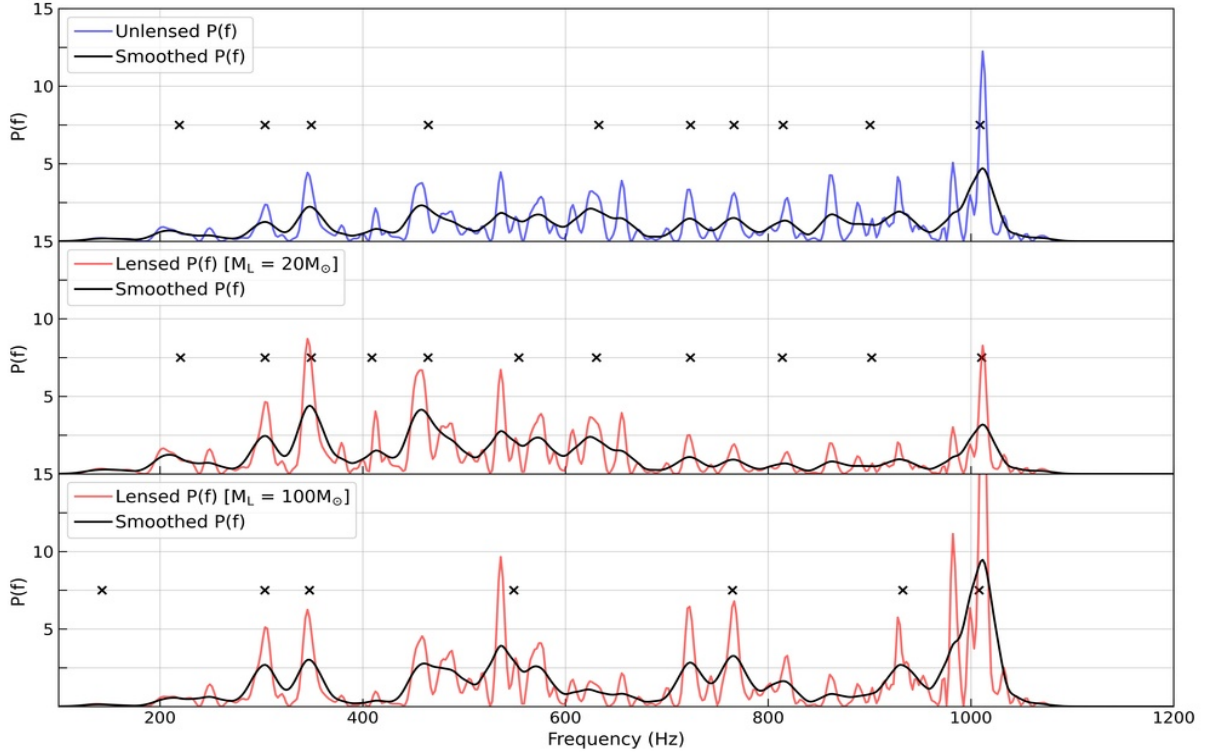


Figure 6. Finding peaks in the power spectrum: In the top panel, the blue line represents power spectrum ($P(f)$) of unlensed signal from Figure 4. The black line represents the smoothed power spectrum using the Savitzky-Golay filter. The ‘x’ points represent the frequency values corresponding to peaks estimated using the algorithm mentioned in the main text. Similarly, in the middle and bottom panel, the red line represents the lensed power spectrum corresponding to a lens mass of $20M_{\odot}$ and $100M_{\odot}$, respectively.

signal. The right panel shows the corresponding power spectra, with the two curves vertically displaced again for better visualisation. The modulus of the amplification factor is shown in black. As can be seen, there is a clear correlation between the power of a lensed signal and oscillations of the amplification factor. The unlensed signal, however, shows no such correlation. We use this correlation as the basis of identifying lensed signals in the following sections.

4. CCSN-like GW Signal

Over the last decade, various multidimensional CCSN simulations have revealed a multitude of information about different processes responsible for the emission of photons, neutrinos, and GWs (e.g., [Dimmelmeier et al., 2008](#); [Scheidegger et al., 2008, 2010](#); [Müller et al., 2013](#); [Cerdá-Durán et al., 2013](#); [Yakunin et al., 2015](#); [Andresen et al., 2017](#); [Morozova et al., 2018](#); [Radice et al., 2019](#); [Andresen et al., 2019](#); [Powell & Müller, 2020](#); [Warren et al., 2020](#); [Vartanyan & Burrows, 2020](#); [Andresen et al., 2021](#)). Unlike chirp signal from merging binaries, the GW signal emitted in

CCSN is broadband in nature covering a frequency range of $\sim(5\text{Hz}, 1500\text{Hz})$. This broadband signal only lasts around one second. The exact numbers depend on the mass and spin of the progenitor star. Following the bounce, there are various processes that give rise to gravitational waves:

1. f-mode and g-mode oscillations of the Proto-Neutron Star (PNS) give rise to waves in the frequency range of a few hundreds to thousand Hertz. The (relative) intensity of waves produced by this method is the highest.
2. The Standing Accretion Shock Instability (SASI), that is formed as a result of the stalling of the shock by the infalling matter, accounts for waves in the region of $\sim 100\text{--}300\text{Hz}$. This is prominent in only those supernovae events where an explosion does not take place. Prompt convection following the bounce also gives rise to waves in the same frequency bracket (for the first ~ 10 milliseconds following the bounce).
3. Asymmetric flow of matter and neutrinos produce waves in the regime of $\sim 0.1\text{--}10\text{Hz}$. The

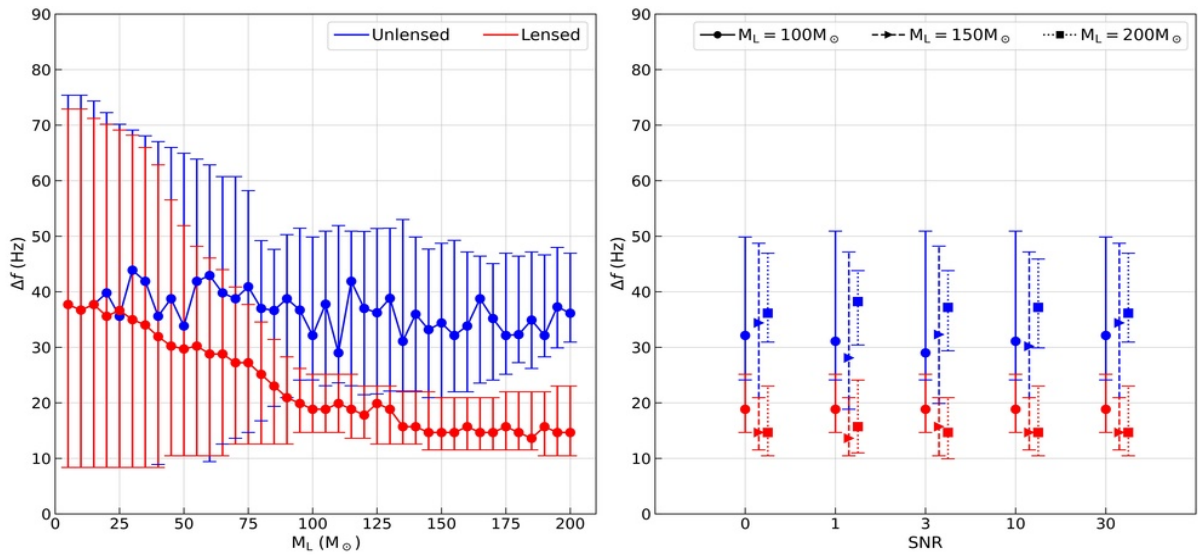


Figure 7. Results of the peak matching method: The left panel represents the efficiency of the peak matching method in the absence of external noise. As elaborated in the main text, Δf is the average distance between peaks of the amplification factor and estimated ‘genuine-peaks’ of the power spectrum. Blue (red) solid points are median values corresponding to unlensed (lensed) signals, and errors bars correspond to 16th and 84th percentiles. The right panel represents the effect of SNR on the median values and error bars for three different mass values as mentioned in the plot legend. A SNR of zero does not mean that there is no signal, but instead refers to the absence of external noise. The various points for different lens masses for a particular SNR value are horizontally shifted for better visualization. One can see that the external noise does not significantly affect the final results.

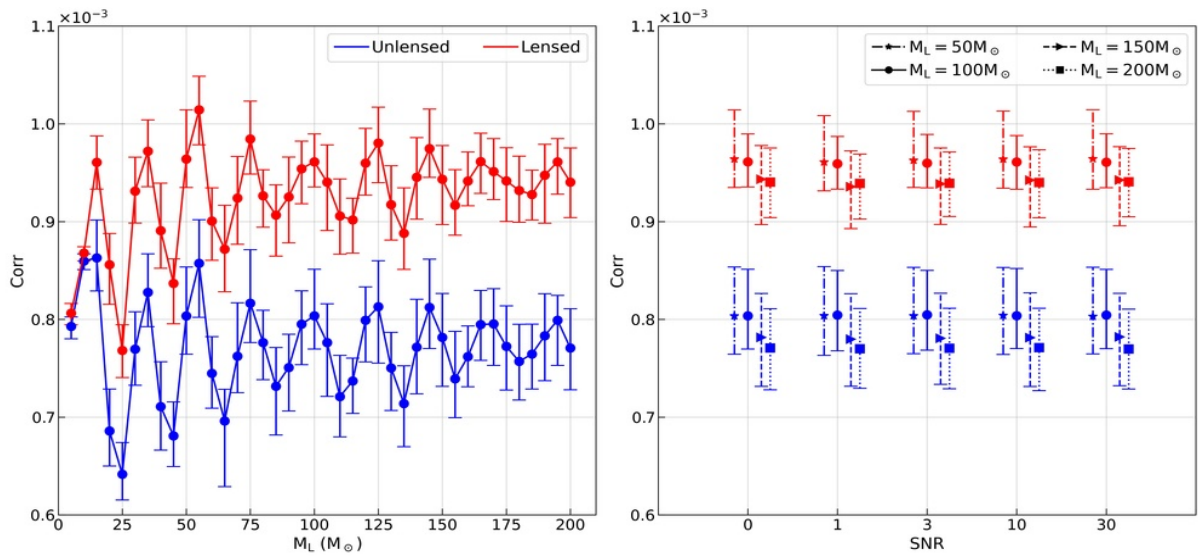


Figure 8. Correlation Integral computed at various lens masses for different cases with varying SNR. Similar to Figure 7, blue (red) solid points are median values corresponding to the unlensed (lensed) signals, and errors bars represent the 16th and 84th percentile values. The left panel represents the correlation values in the absence of external noise. The effect of external noise is presented in the right panel for three different lens mass values. Similar to the peak matching algorithm, the external noise does not play a significant role in the correlation integral values.

strain produced here is the weakest amongst the various processes highlighted here.

Owing to the variety of processes involved in the production of GWs, these signals may offer a multi-

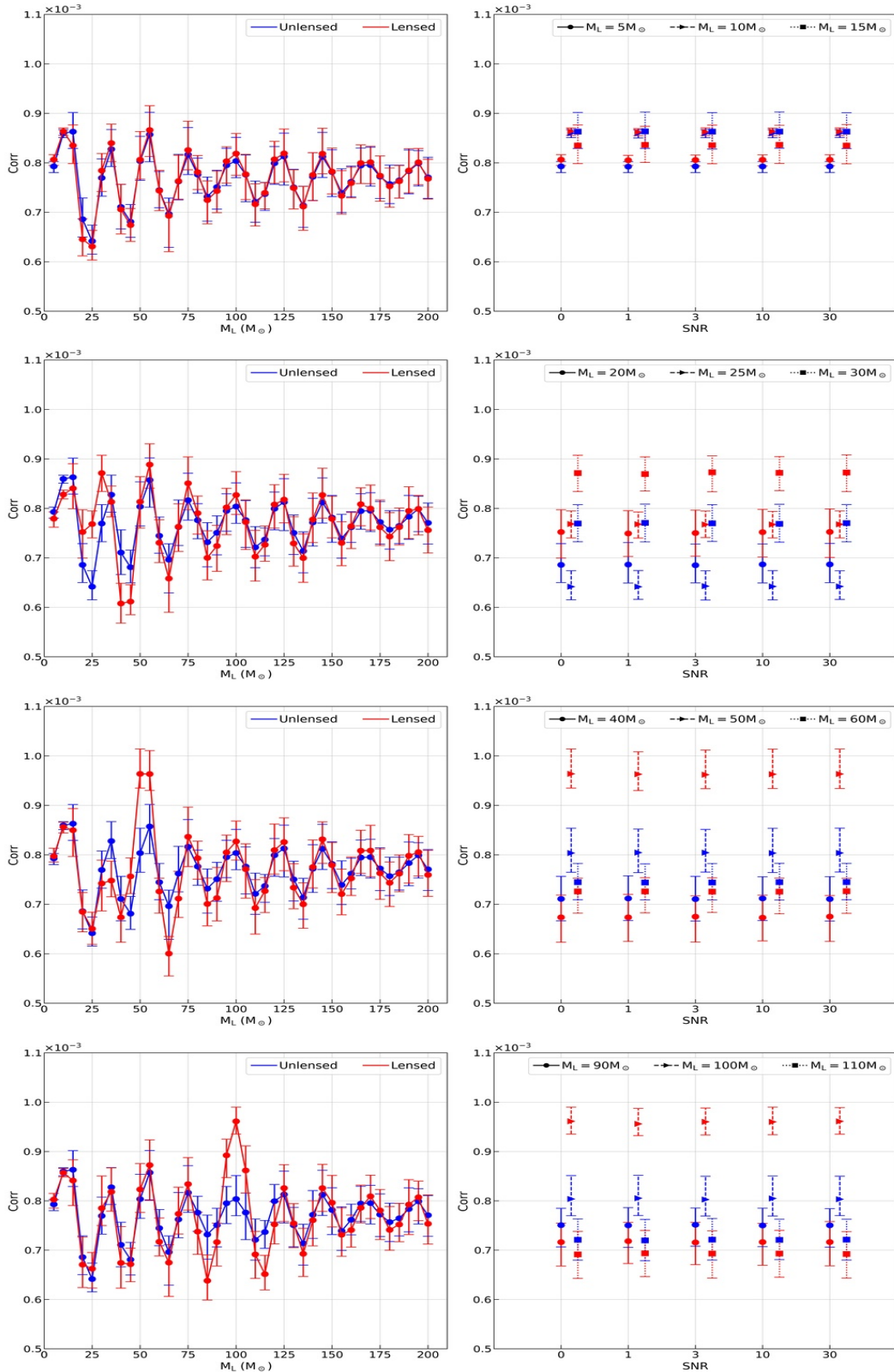


Figure 9. Using the Correlation Integral to estimate M_L at known $y(=1)$: Top to bottom, the signals are lensed by a 5, 25, 50 and $100 M_\odot$ lens respectively. The correlation integral is computed by assuming different values of M_L as indicated on the x-axis. Blue (red) points correspond to unlensed (lensed) signals, solid points are median values, and errors bars correspond to 16th and 84th percentiles. Similar to Figures 7 and 8, the left panels correspond to the case without any external noise. The right panel represents the effect of different SNR values near the actual lens mass value. As has been shown in Figure 8, this method is able to differentiate between lensed and unlensed signals only for $M_L \geq 15 M_\odot$, and while estimates of M_L can be made in this regime, the estimates are not always accurate unless $M_L \geq 50 M_\odot$.

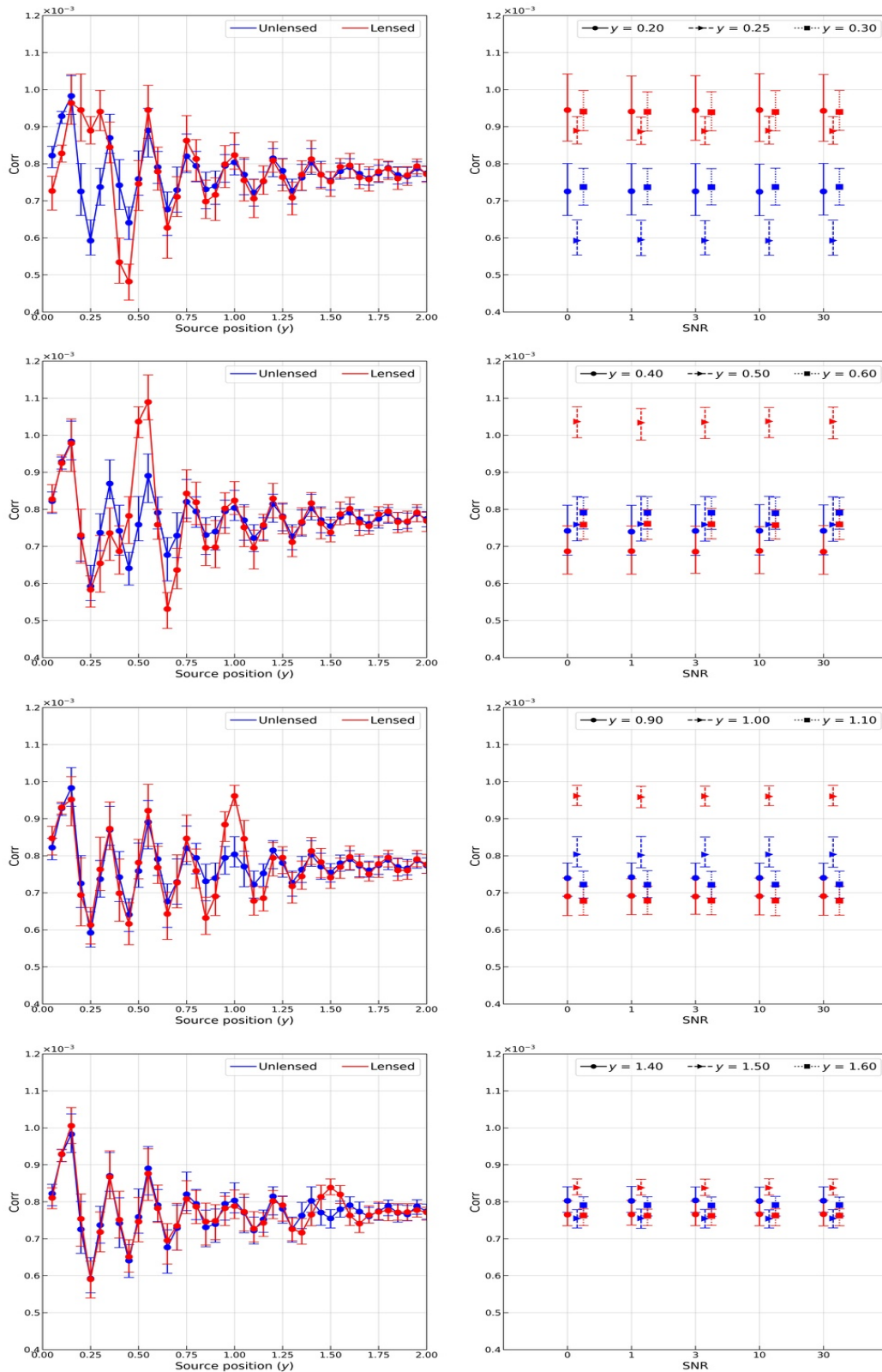


Figure 10. Using the Correlation Integral to estimate y at known $M_L (= 100M_\odot)$: Top to bottom, the signals are lensed by assuming the source to be present at $y = 0.25, 0.5, 1.0$ and 1.5 respectively. The correlation integral is computed by assuming different values of y as indicated on the x-axis. Blue (red) points correspond to unlensed (lensed) signals, solid points are median values, and errors bars correspond to 16th and 84th percentiles. The rest of the details are similar to Figure 9.

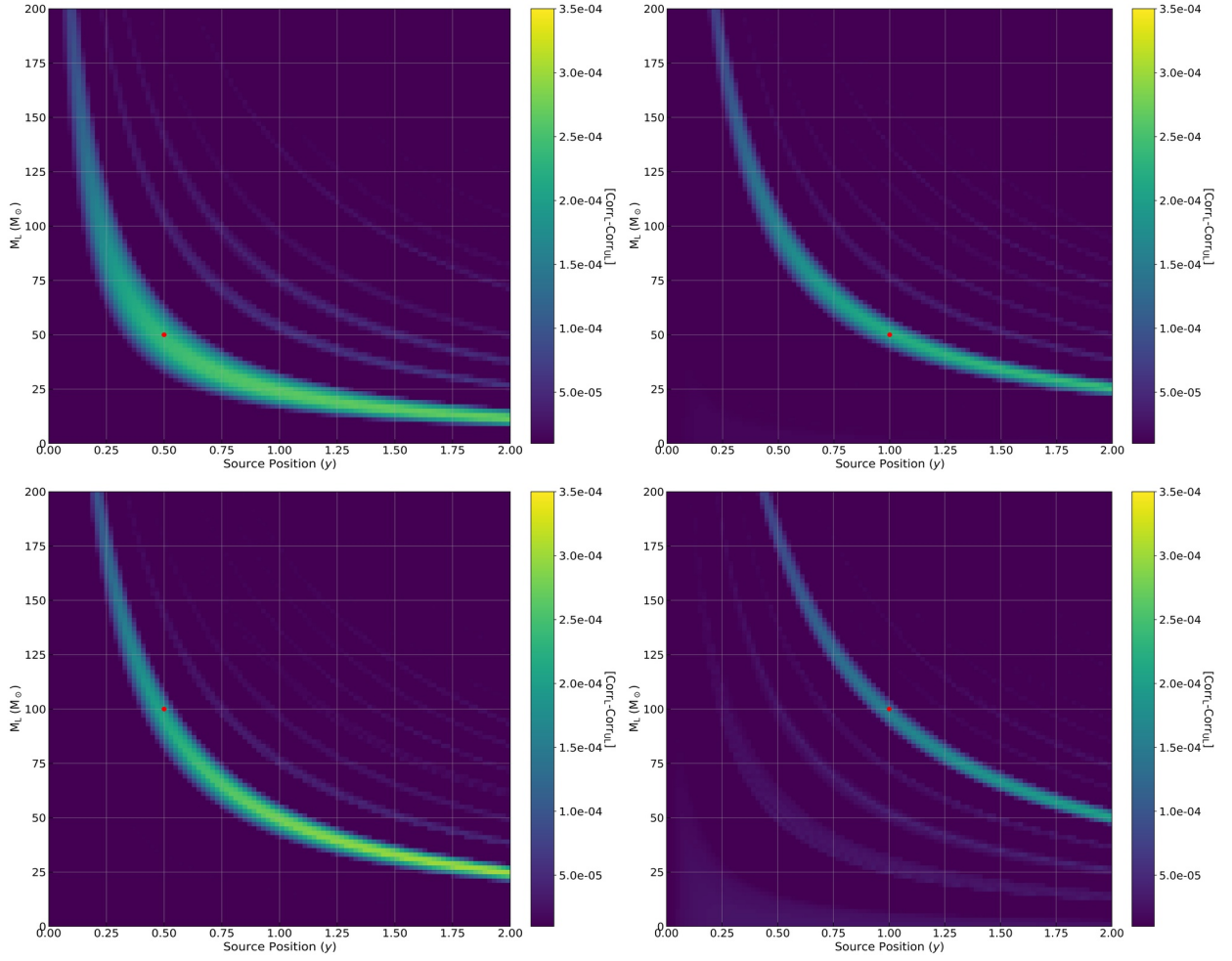


Figure 11. Contour plots for the median value of the correlation integral: In each panel, the reference signal is lensed by the parameter values denoted by the red dot. The correlation integral for the (reference) lensed and unlensed signal is computed by assuming the lens parameters as denoted by the corresponding x- and y-axis values. Each panel shows the difference of correlation values between lensed and unlensed signal.

dimensional probe into CCSN events. For instance, the ratio of the progenitor star’s core kinetic to potential energy, post bounce oscillation frequency of the proto-neutron star (Afle & Brown, 2021), CCSN explosion mechanism (Powell *et al.*, 2016), angular momentum of the progenitor (Abdikamalov *et al.*, 2014), and the nuclear equation of state (Edwards, 2021) are some of the many properties that can potentially be surmised from the observed gravitational waves.

Despite all the above known information, it is not straightforward to develop templates for the CCSN GW signals like merging binaries. In our current work, we use a simple approach (described below) to generate CCSN-like mock GW signals. We start with a Gaussian Random Field in the frequency domain with Power Spectrum $P(f)$:

$$h(f_j) = (a_j + b_j) \sqrt{P(f_j)}, \quad (2)$$

where, a_j and b_j represent random numbers drawn from a unit Gaussian distribution. To generate the corresponding time-domain signal, we use the following relation:

$$h(t) = \int_{(f_0-3\sigma_f)}^{(f_0+3\sigma_f)} h(f) \exp[-2\pi i f t - (f - f_0)^2 / (2\sigma_f^2)] \Delta f, \quad (3)$$

where, $f_0 \equiv f_0(t)$ is the central frequency, and $\sigma_f \equiv \sigma_f(t)$ is a measure of the spread of the signal (in frequency domain) around the central frequency. This time dependent filtering scheme removes contribution of frequencies far away from $f_0(t)$ where the frequency separation is quantified in units of $\sigma(t)$. These functions can be used to model variation of the signal in frequency space as a function of time. Following Equation 3, we choose values such that the central frequency (f_0) of the signal increases linearly from 100 Hz to 1000 Hz

in a span of 0.4 seconds. After that, the signal stabilizes at 1000 Hz. The spread of signal (σ_f) increases linearly from 25 Hz to 100 Hz during the first half of the signal, and drops linearly from 100 Hz to 25 Hz during the second half.

Figure 4 represents one example of a CCSN-like signal generated using the above described method. The left panel shows the signal in time domain with time on x-axis and signal strain on y-axis. The right panel represents the corresponding (time-frequency) spectrogram. One can notice the linear increase between time and frequency and the saturation above 0.4 seconds.

5. Results

In this section, we present our results of analysis of gravitational lensing of CCSN-like mock GW signals generated using the method described in §4.

5.1 Lensed CCSN Signal

The current and upcoming GW detectors cannot detect the cosmological CCSN GW signals. Only signals coming from within our own Galaxy or the nearby satellite galaxies are likely to be detected. Hence it is the stellar mass compact objects that can introduce the lensing effects in these CCSN GW signals which can be very well approximated by a point mass lens (see Appendix A. for further details). In principle one can consider intermediate mass black holes but the number of such objects is expected to be very small.

In Figure 5, we present two lensed CCSN-like GW signals. The top left (right) panel represents the lensed and unlensed signals in red and blue, respectively, with a lens of $20M_\odot$ ($100M_\odot$). As has been discussed in §3., one can see that the lensing introduces both amplification and de-amplification based on the frequency value of the signal. Lensing also shifts the signal in time (phase shift) although not visible in this plot but it can be inferred from Figure 1 or Figure 2. The bottom left (right) panels represent the power spectrum of lensed and unlensed with lens mass $20M_\odot$ ($100M_\odot$). The solid black line represents the amplification factor ($|F|$) due to the lens mass. One can clearly see a correlation between the amplification factor ($|F|$) and the amplitude of peaks in the corresponding (lensed) power spectrum: in the power spectra of lensed signals, peaks at frequencies surrounding maximas of the amplification factor are amplified, and peaks at frequencies surrounding minimas of the amplification factor are de-amplified. No such trend is observed for power spectra of unlensed signals.

5.2 Identifying a Lensed Signal

5.2.1 Tracking Oscillations in Power Spectra While the power spectrum seems to be a promising tool to track down a lensing event, one would like to know how efficient this method is, or whether any statistical statements can be made about using such a method. One way to address this question is to estimate the average distance between a peak of the amplification factor and the closest peak of the power spectrum. One can alternatively focus on the correlation between troughs in the amplification factor and the observed signal. Both these methods yield qualitatively similar results. We first discuss an approach based on the peaks alone. There is one main problem with the proposed method: owing to the stochastic nature of the signal, there are a large number of ‘false peaks’, i.e. peaks arising as a result of the randomness associated with the signal (in our case, this arises due to the white noise power spectrum and the Gaussian random field), in both the lensed and unlensed power spectra, which would naturally bias our results. If external noise is present, this adds to the number of apparent peaks, which may further bias our results.

To tackle the above-mentioned issue of false-peaks, we employ the following method to estimate ‘genuine peaks’: we first use a Savitzky-Golay filter (Savitzky & Golay, 1964, hereafter SAVGOL) with a bin size of $N = 11$ to smoothen out the power spectrum. Although arbitrary, the value of N is important: if N is too small, the smoothened curve retains a large amount of randomness of the signal, while if N is too large, the number (location) of peaks drastically reduces (shifts). After experimenting with a few different values, we find that $N = 11$ works well, and we hence proceed with this. For the highest peak of the smoothened power spectrum, we traverse to higher and lower frequencies such that the power is half of the power at the peak. The location of the peak is then estimated as a weighted average across the bounded region obtained above: $f_{pk} = \frac{\sum P(f)f}{\sum P(f)}$. We repeat this process for all other peaks, selecting peaks in descending order. Figure 6 shows the results of the above peak finding algorithm for the power spectrum of the unlensed signal from Figure 4. The top panel in Figure 6 represents the power spectrum of the unlensed signal in blue and the corresponding smoothed power spectrum in black. The middle (lower) panel represents the lensed and smoothed power spectrum for the case with a lens mass of $20M_\odot$ ($100M_\odot$). The black ‘x’ symbols represent the frequency values corresponding to the peaks estimated using the above mentioned algorithm. Relative to estimated peaks of the unlensed signal, one can see that the lensing due to a $20M_\odot$ lens increases the number of peaks in the $<600\text{Hz}$ range, whereas the number of peaks are reduced in $>600\text{Hz}$ region. The same is true

for lensing due to a $100M_{\odot}$ lens, although in different frequency regions due to rapid oscillations of the corresponding amplification factor. Overall, the number of peaks of the original power spectrum is reduced considerably, which helps counter the bias of randomness of the signal, at least partially. Throughout the rest of the paper, we continue to refer to peaks identified using this algorithm as ‘genuine peaks’.

We now proceed to check the efficiency of the previously described power spectrum method to identify lensing: we generate 100 mock signals using the method outlined in §4., all with the same power spectrum. For each signal, we estimate the average distance between peaks of the amplification factor and estimated ‘genuine-peaks’ of the power spectrum, for both lensed and unlensed signals. This quantity is denoted by Δf in Figure 7. Blue (red) points correspond to the results of the unlensed (lensed) signals, the solid points are median values, and the error bars correspond to 16th and 84th percentiles. We consider multiple cases with varying amounts of external white noise injected into the mock signal. Since our method is not optimized to identify instrumental noise, we include time-independent white noise representing instrumental noise only in the same frequency range where the original signal is present, i.e. in the frequency range $\sim[100\text{Hz}, 1100\text{Hz}]$. This ensures that our results are not biased by those regions which only contain external noise. We begin by analyzing the case with no external noise (left panel of Figure 7), and later extend the discussion to the other cases (right panel of Figure 7). As one can see from the left panel, for relatively less massive lenses, the median values are well within the two percentile regions. As the mass of the lens is increased, the two median values separate out from the percentile regions (at $\sim 100M_{\odot}$), and ultimately for higher masses, the two percentile regions decouple as well (at $\sim 150M_{\odot}$). This shows that although the outlined power spectrum tool is useful, it is dependable only for high mass lenses ($>150M_{\odot}$). This corresponds to cases where the amplification factor undergoes multiple oscillations within the frequency-range of the signal, and hence a greater number of (more rapid) oscillations are observed in the power spectrum of the (lensed) signal. It is for the same reason that the error bars begin to diminish as M_L increases: for heavier lenses, since there are a greater number of maximas in the considered frequency range, the number of ‘distances’ under consideration is larger. Computing the average of a greater number of ‘distances’ would smoothen out the variation, resulting in tighter error bars. While this argument holds for both lensed and unlensed signals, there is one difference: we observe a greater number of ‘true’ peaks for the lensed signal, while we observe ‘random’

peaks for the unlensed signal. That is why we observe a steady decrease with the median values of the lensed signal, while the median values of the unlensed signal oscillate randomly. As noted earlier, this stochastic behavior (of the unlensed signals) stems from the randomness associated with the original signal.

We next proceed to see whether our power spectrum method is able to identify lensed signals when external noise is present in the signal as well (right panel of Figure 7). Although this plot demonstrates trends for only three different values of M_L , the following discussion takes all other masses (shown in the left panel) into account as well. For $\text{SNR} = 30$, the results are identical to those corresponding to case with no added noise. For $\text{SNR} = 10$, we note differences for the lensed results only at small values of M_L . This is expected, as these are the regions where trends carry the imprint of the inherent randomness of the signal. However, the results of the unlensed signal show variations at all values of M_L . For smaller values of SNR , the median values show some variation for both lensed and unlensed signals at all lens masses. Despite the variation, at large M_L , the median lensed values are all comparable to each other. With the percentile regions, we note an important difference between low and high SNR scenarios: for high SNR (10 and 30), the two percentile regions begin to separate out at $150M_{\odot}$, which is consistent with the case with no external noise. However, this separation is observed at $155M_{\odot}$ ($160M_{\odot}$) for the case with $\text{SNR} = 3$ ($\text{SNR} = 1$). We attribute this to the excess noise that pollutes the features of the power spectrum.

5.2.2 Correlation Integral While studying the average distance between the peaks of the power spectrum and amplification factor is one way to proceed, one may also look at the correlation integral between the amplification factor and the power spectrum. Specifically, the following integral can be studied:

$$\text{Corr} := \frac{\int df P(f)|F|^2(f)}{\left[\int df P(f)\right]\left[\int df |F(f)|^2\right]}, \quad (1)$$

where $P(f)$ is the power spectrum and $|F(f)|$ is the absolute value of the amplification factor at a given frequency value f . The advantage is that we do not have to use any techniques to estimate genuine peaks of the power spectrum. The left panel of Figure 8 shows the above integral estimated at different values of M_L for the case with no external noise. As in Figure 7, blue (red) points correspond to the results of the unlensed (lensed) signals, the solid points are median values, and the error bars correspond to 16th and 84th percentiles. As can be seen, except for $M_L \leq 10M_{\odot}$, there is a clear

offset between the median values of the lensed and unlensed signals, and the percentile regions are well separated as well. While an oscillatory behavior is expected for the median values of the unlensed signals, one expects the median values of the lensed signals to increase monotonically with lens mass, since the power spectrum displays more rapid oscillations at higher values of M_L . Instead, we observe that the correlation integral for the lensed signals rise to a point, and more or less flatten out. We attribute this behaviour to the randomness of the CCSN-like GW signal. In the right panel, we consider multiple cases with varying values of SNR, and follow the same procedure to inject time-independent white noise as outlined in the previous Subsection 5.2.1. Once again, we show results only for three values of M_L , but the following statement holds true for all other cases as well: the results remain more or less the same for a wide range of values of SNR, and the variation between cases with different SNR is smaller than the variation observed in the previous peak-matching method.

5.3 Constraining Point Mass Lens Parameters

While the two methods outlined above offer possible avenues to identify lensed signals, they require a priori knowledge of the behaviour of the amplification factor. For an isolated point mass lens, this corresponds to knowing the values of the lens mass (M_L) and the source position (y). While this stands true for the peak matching method, the correlation integral method is able to identify lensed signals even in cases where an estimate of M_L is not available, as long as y is known. To demonstrate this, in Figure 9, from top to bottom, we consider signals to be lensed by a 5, 25, 50 and 100 M_\odot lens respectively. In all cases, we fix $y = 1$. The correlation integral is estimated at multiple values of M_L , as indicated on the x-axis. Consistent with our observations from Figure 8, this method is not able to identify lensing when $M_L \leq 10M_\odot$. From the bottom two panels, we notice that the correlation integral peaks near the true value of M_L . It is also only around the true value of M_L that (a) there is a significant difference between the correlation of lensed and unlensed signals, and (b) the percentile regions of the lensed and unlensed signals separate out. We also note that there is a relatively sharp drop in the correlation on either side of the peak. In addition to identifying lensed signals, such an approach may be useful to obtain an estimate of M_L .

In the second panel from the top, although the correlation integral does peak around the true value of M_L , the peak is not a global maxima. As can be seen from the plot, the reason for the same is that the (median) correlation integral of the unlensed signals corresponding to the true value of M_L ($=25M_\odot$) is a minima. It

thus seems that the accuracy of the estimate of M_L depends on the value of the correlation integral of the unlensed signals, at least for small M_L . From Figure 8, for $M_L \geq 50M_\odot$, we see that the (median) correlation integral of all lensed signals is always greater than the *maximum* (median) correlation integral of unlensed signals. For $M_L \geq 50M_\odot$, a global maxima will hence be present when one tries to make a plot similar to Figure 9. Thus, while it may be possible to estimate M_L for $M_L > 10M_\odot$, the estimate may not always be accurate unless $M_L \geq 50M_\odot$. Especially for $10M_\odot < M_L < 50M_\odot$, in addition to locating maximas, it may be useful to check if there is a sharp drop in the correlation on either side of the peak. This may provide additional hints as to whether one is close to the true value of M_L . At this juncture, we find it important to state the following point: the above mentioned ‘limits’ of $10M_\odot$ and $50M_\odot$ were obtained with y fixed at 1. Since the amplification factor oscillates slower (faster) for smaller (larger) values of y , the above mentioned limits would be larger (smaller) for smaller (larger) values of y . Note that the value of y will similarly affect the ‘limits’ of the peak-matching method as well.

Another case that one can consider is when an estimate of M_L is available, but y is unknown. Figure 10 explores this scenario. From top to bottom, we consider the source to be positioned at $y = 0.25, 0.5, 1.0$ and 1.5 respectively. In all cases, we fix $M_L = 100M_\odot$. The correlation integral is estimated at multiple values of y , as indicated on the x-axis. Although the percentile regions of the lensed and unlensed signals separate close to the actual value of y , other regions also show significant separation between lensed and unlensed signals (for example $y = 0.25, 0.50$ cases). Such an observation indicates the possible degeneracies in the lens parameter values.

The final case that we explore is a rather extreme one in which both M_L and y are unknown. In Figure 11, we see if the correlation integral method can be used for performing estimation of these two parameter simultaneously. In each panel, the reference signal is lensed using parameters denoted by the red dot. The correlation integral is computed by assuming various lens parameters as denoted by the corresponding x- and y-axis values. Figure 11 shows the median value of the correlation integral. Note that no external noise is injected into any of these signals. In each panel, the value of difference of correlation integral between lensed and unlensed signal is plotted, i.e., $[\text{Corr}_{\text{Lensed}} - \text{Corr}_{\text{Unlensed}}]$. Figure 11 is a two-dimensional analog of Figure 9 and 10. While the true set of parameters is always close to contours with high values of the correlation integral, the contours are not tight enough to provide a reasonable estimate of the two parameters. This is due to the

degeneracies between the two parameters. Such a result is also expected from Figure 1, where we have shown the amplification curves while fixing one of these parameters. From the top-left panel, one can see that if both y and M_L have small values, then it can be tough to end up near the actual values as the lensing does not introduce significant changes in the signal. Even if we do increase the mass of the lens, the banana shape of the contours allows a wide range of the lens parameters. Hence, we do not expect to tightly constrain both parameters simultaneously in most cases.

5.4 Limitations of our Methods

We have considered two methods to establish presence of gravitational lensing. The proposed peak-matching method is reliable only for massive lenses ($M_L > 150M_\odot$). The correlation integral method is able to differentiate between lensed and unlensed signals starting at $M_L \sim 15M_\odot$, but even such lenses are unfortunately not very abundant. For a supernova within the galactic plane, juxtaposition of multiple lenses may lead to a high effective value for the lens mass. Apart from this limitation, we summarise a few other limitations of our methods.

In the previous subsection, we have introduced a possible method to estimate genuine peaks. Peaks identified using this method seem to provide results that are well aligned with what one would intuitively expect, at least for massive lenses. However, we note that this proposed method is not entirely foolproof: when one chooses to create a bounded region around each peak such that the power within the region is within 50% of the value of the peak, the number of estimated peaks remains more or less constant across all signals. As the mass of the lens increases, the number of peaks corresponding to the amplification factor increase, and at some point, the number of peaks of the amplification factor equals the number of estimated peaks of the power spectrum. For lens masses above this limit, the value of Δf will worsen due to the limited number of peaks. This is the reason why the upper limit of the error bar widens for the last few (lensed) data points in Figure 7. In such a case, we have to explore whether changing the smoothing scale (number of bins) or the level up to which we average (half power in the results presented here) the signal has an impact.

Another way to reduce the number of false peaks is to consider only those peaks of the smoothed power spectrum that are larger than a given lower threshold (for e.g., three times the rms value). However, introducing such a threshold seems to greatly reduce the number of peaks estimated using our method, and the values of Δf are biased as a result. In our discussion, we have only considered white noise as external noise.

By definition, white noise has almost equal power at all frequencies. In real life observations, noise follows a different power spectrum as different sources of noise dominate for different frequencies. Modelling with frequency dependent noise is required to study if it introduces any non-trivial effects. However, as the instrument noise does not have any oscillatory behaviour in frequency, we do not expect any significant changes.

It is noteworthy that the error bars in Figure 7 are asymmetric with respect to the median value. This arises due to the limited resolution of the power spectrum: the resolution here is $\sim 2\text{Hz}$, because of which there is a bias with respect to the number of ‘small values’ of distances between maximas of the amplification factor and peaks of the power spectrum that are observed. This leads to error bars that are shorter on the lower end, which are noticeable when the median value of Δf is relatively small. Zero-padding the signal before computing the power spectrum helps in improving frequency resolution, but this dilutes the number/location of peaks. In addition, during real-life observations, where sampling frequency of the detector in time domain is limited, features of the power spectrum may not always be well reproduced.

An alternate approach to identify lensing is the correlation integral. As already noted, the advantage here is that one does not have to worry about identifying genuine peaks. This method seems to work well as long as the frequency range analyzed contains both the ‘actual’ signal and external noise. If the analyzed frequency range contains a sub-range in which only external noise is present, the correlation will reduce. While performing such an analysis, it is thus important to identify the frequency range in which the ‘actual’ signal is present, and compute the correlation only in this ‘isolated’ region. For example, the current LIGO band covers the frequency range of a few tens of Hertz to a few thousand Hertz, and when a signal is detected, the observed signal (‘actual’ signal + external noise) would cover a majority of this band. However, if the actual signal is present only in the frequency range of $\sim [100\text{Hz}, 1100\text{Hz}]$, the correlation is to be computed only in this range. Unfortunately, this can be reliably performed only when the SNR is high. Such isolation is required for the peak matching method as well. Further studies are required to explore limitations arising from this aspect.

6. Conclusions

We have discussed gravitational lensing of wavepackets and broad band gravitational wave signals in this paper. We have shown the expected effects of micro-lensing

on the amplitude and phases. We have demonstrated that the power spectrum of the observed signal is a useful quantity in the analysis of signal from sources such as core collapse supernovae.

We have described two possible methods to identify lensing in cases where our knowledge of the waveform and power spectrum is limited. Specifically, we have studied cases where the wave nature of radiation is important during gravitational lensing. Lensing in this regime is chromatic, and different frequency components are amplified/de-amplified by varied factors, as governed by the oscillations of the amplification factor. This gives rise to oscillations in the power spectrum of a lensed signal. Our proposed methods rely on studying such oscillations. When the waveform under consideration is broadband and incoherent, as is the case with a CCSN GW signal, comparison of peaks between power spectra and the amplification factor is unfortunately dependable only for massive lenses. This is due to the presence of peaks in the power spectrum due to randomness. To partially overcome this problem, we employed a possible method to estimate ‘genuine peaks’. This certainly offers an improvement over directly selecting peaks from the power spectrum. However, as has already been noted, this method is not always robust, and alternate algorithms are required for better analysis.

We have demonstrated that the correlation integral is a powerful tool to identify gravitational lensing. This is capable of doing so reliably for lens masses as low as $15 M_{\odot}$. Most importantly, this is insensitive to the presence of noise. We have shown that in principle we can infer parameters of the lens using the correlation integral though this is not always reliable if both the lens mass and displacement y are unknown. In the GAIA era, it may be possible to get at least partial information about the lens if the source is detected using electromagnetic waves as well and is localized on the sky.

The rate of SNe in the Large Magellanic Cloud (LMC), the Small Magellanic Cloud (SMC) and within the Galaxy is $\sim 1/200$ year (Bozzetto *et al.*, 2017), $\sim 1/500$ year (Vink, 2020) and $\sim 2/100$ year (Adams *et al.*, 2013), respectively. In addition, the microlensing optical depth for LMC/SMC is $\sim 10^{-7}$ (e.g., Bennett, 2005; Moniez, 2010; Wyrzykowski *et al.*, 2011), whereas the microlensing optical depth within the Galaxy peaks in the Galactic plane ($\sim 10^{-6}$) and continuously decreases at high latitudes (e.g., Mróz *et al.*, 2019, 2020). Hence, the chances of observing a microlensed SNe are similar within the Galaxy and the Magellanic Clouds, although all cases lead to very small optical depths for microlensed SNe.

The power spectrum method can be applied to any broad band signal and is especially useful for incoher-

ent signals where the phase information is not available from models.

Acknowledgements

RR would like to thank Ambresh Shivaji for helpful discussions and comments. RR also thanks the Department of Science and Technology, Government of India for being awarded the INSPIRE scholarship. AKM would like to thank Council of Scientific and Industrial Research (CSIR) India for financial support through research fellowship No. 524007. Authors thank the anonymous referee for insightful comments. Authors acknowledge the use of IISER Mohali HPC facility. This research has made use of NASA’s Astrophysics Data System Bibliographic Services.

References

- Abbott, B. P., Abbott, R., Abbott, T. D., *et al.* 2019, Physical Review X, 9, 031040
- Abbott, R., Abbott, T. D., Abraham, S., *et al.* 2020, arXiv e-prints, arXiv:2010.14527
- Abdikamalov, E., Gossan, S., DeMaio, A. M., & Ott, C. D. 2014, Phys. Rev. D, 90, 044001
- Adams, S. M., Kochanek, C. S., Beacom, J. F., Vagins, M. R., & Stanek, K. Z. 2013, ApJ, 778, 164
- Afle, C., & Brown, D. A. 2021, Phys. Rev. D, 103, 023005
- Andresen, H., Glas, R., & Janka, H. T. 2021, MNRAS, 503, 3552
- Andresen, H., Müller, B., Müller, E., & Janka, H. T. 2017, MNRAS, 468, 2032
- Andresen, H., Müller, E., Janka, H. T., *et al.* 2019, MNRAS, 486, 2238
- Bennett, D. P. 2005, ApJ, 633, 906
- Bozzetto, L. M., Filipović, M. D., Vukotić, B., *et al.* 2017, ApJS, 230, 2
- Broadhurst, T., Diego, J. M., & Smoot, George, I. 2018, arXiv e-prints, arXiv:1802.05273
- Cerdá-Durán, P., DeBrye, N., Aloy, M. A., Font, J. A., & Obergaulinger, M. 2013, ApJ, 779, L18
- Christian, P., Vitale, S., & Loeb, A. 2018, Phys. Rev. D, 98, 103022

- Diego, J. M., Hannuksela, O. A., Kelly, P. L., *et al.* 2019, *A&A*, 627, A130
- Dimmelmeier, H., Ott, C. D., Marek, A., & Janka, H. T. 2008, *Phys. Rev. D*, 78, 064056
- Edwards, M. C. 2021, *Phys. Rev. D*, 103, 024025
- Eker, Z., Bakış, V., Bilir, S., *et al.* 2018, *Monthly Notices of the Royal Astronomical Society*, 479, 5491–5511
- Fryer, C. L., Holz, D. E., & Hughes, S. A. 2002, *ApJ*, 565, 430
- Fryer, C. L., & New, K. C. B. 2011, *Living Reviews in Relativity*, 14, 1
- Haris, K., Mehta, A. K., Kumar, S., Venumadhav, T., & Ajith, P. 2018, *arXiv e-prints*, arXiv:1807.07062
- Kuroda, T., Takiwaki, T., & Kotake, K. 2014, *Phys. Rev. D*, 89, 044011
- Li, S.-S., Mao, S., Zhao, Y., & Lu, Y. 2018, *MNRAS*, 476, 2220
- Meena, A. K., & Bagla, J. S. 2020, *MNRAS*, 492, 1127
- Mishra, A., Meena, A. K., More, A., Bose, S., & Singh Bagla, J. 2021, *arXiv e-prints*, arXiv:2102.03946
- Moniez, M. 2010, *General Relativity and Gravitation*, 42, 2047
- Morozova, V., Radice, D., Burrows, A., & Vartanyan, D. 2018, *ApJ*, 861, 10
- Mróz, P., Udalski, A., Skowron, J., *et al.* 2019, *ApJS*, 244, 29
- Mróz, P., Udalski, A., Szymański, M. K., *et al.* 2020, *ApJS*, 249, 16
- Müller, B., Janka, H.-T., & Marek, A. 2013, *ApJ*, 766, 43
- Nakamura, T. T., & Deguchi, S. 1999, *Progress of Theoretical Physics Supplement*, 133, 137
- Ohanian, H. C. 1974, *International Journal of Theoretical Physics*, 9, 425
- Ott, C. D. 2009, *Classical and Quantum Gravity*, 26, 063001
- Ott, C. D., Burrows, A., Dessart, L., & Livne, E. 2006, *Phys. Rev. Lett.*, 96, 201102
- Ott, C. D., Abdikamalov, E., Mösta, P., *et al.* 2013, *ApJ*, 768, 115
- Peters, P. C. 1974, *Phys. Rev. D*, 9, 2207
- Piro, A. L., & Pfahl, E. 2007, *ApJ*, 658, 1173
- Powell, J., Gossan, S. E., Logue, J., & Heng, I. S. 2016, *Phys. Rev. D*, 94, 123012
- Powell, J., & Müller, B. 2020, *MNRAS*, 494, 4665
- Radice, D., Morozova, V., Burrows, A., Vartanyan, D., & Nagakura, H. 2019, *ApJ*, 876, L9
- Savitzky, A., & Golay, M. J. E. 1964, *Analytical Chemistry*, 36, 1627
- Scheidegger, S., Fischer, T., Whitehouse, S. C., & Liebendörfer, M. 2008, *A&A*, 490, 231
- Scheidegger, S., Whitehouse, S. C., Käppeli, R., & Liebendörfer, M. 2010, *Classical and Quantum Gravity*, 27, 114101
- Schneider, P., Ehlers, J., & Falco, E. E. 1992, *Gravitational Lenses*, doi:10.1007/978-3-662-03758-4
- Somiya, K. 2012, *Classical and Quantum Gravity*, 29, 124007
- Sotani, H., Takiwaki, T., & Togashi, H. 2021, *arXiv e-prints*, arXiv:2110.03131
- Suyama, T., Takahashi, R., & Michikoshi, S. 2005, *Physical Review D*, 72, doi:10.1103/physrevd.72.043001
- Takahashi, R., & Nakamura, T. 2003, *ApJ*, 595, 1039
- Unnikrishnan, C. S. 2013, *International Journal of Modern Physics D*, 22, 1341010
- Vartanyan, D., & Burrows, A. 2020, *ApJ*, 901, 108
- Vink, J. 2020, *Physics and Evolution of Supernova Remnants* (Springer)
- Warren, M. L., Couch, S. M., O'Connor, E. P., & Morozova, V. 2020, *ApJ*, 898, 139
- Wyrzykowski, L., Skowron, J., Kozłowski, S., *et al.* 2011, *MNRAS*, 416, 2949
- Xu, F., Ezquiaga, J. M., & Holz, D. E. 2021, *arXiv e-prints*, arXiv:2105.14390
- Yakunin, K. N., Mezzacappa, A., Marronetti, P., *et al.* 2015, *Phys. Rev. D*, 92, 084040

Appendix A. How Good is the Point-Mass Approximation?

A straightforward generalization to the point mass approximation is to model the microlens as a uniform-density sphere of radius R_\star . The corresponding three-dimensional gravitational potential is given as

$$\phi(r) = \begin{cases} -\frac{GM}{2R_\star} \left(3 - \frac{r^2}{R_\star^2} \right) & ; r \leq R_\star, \\ -\frac{GM}{R_\star} & ; r \geq R_\star, \end{cases} \quad (\text{A1})$$

and the corresponding projected gravitational lensing potential is given as (Suyama *et al.*, 2005)

$$\psi(x) = \begin{cases} \ln[1 + (1 - (x/R)^2)^{0.5}] \\ \quad - (1/3)[4 - (x/R)^2][1 - (x/R)]^{0.5} & ; x \leq R, \\ \ln[x/R] & ; x \geq R, \end{cases} \quad (\text{A2})$$

where $R=R_\star/\xi_0$ is the radius of the lens normalised by the Einstein radius ($=\sqrt{4GM_L D_d D_{ds}/c^2 D_s}$) of the Lens system. It turns out that this (dimensionless) parameter R is what determines the accuracy of the point mass approximation.

In Figure 12, we shows the absolute and phase values of the amplification factor for a point mass lens and uniform density sphere lenses. When the radius of the lens is $R \sim 0.1$ (or even smaller), the point mass lens approximation leads to very accurate results. However, as the radius increases ($R \sim 0.4 - 0.5$), we begin to notice discrepancies between the two models at high frequency values. For even larger values of lens radius, the point mass lens approximation no longer holds.

To assess the physical situations during which the point mass approximation holds, we next provide certain ballpark numbers for the value of R :

1. For a lens system in which all distances are of the order of one kpc, and for a solar mass lens, the Einstein radius is of the order of 10^{-9} rad. The angular size of the sun at this distance is $\sim 10^{-11}$ rad, and thus $R \sim 0.01$. Hence for typical galactic distances, a solar mass lens is well approximated by a point mass lens.
2. For stars on the Main Sequence, $R_\star \propto M^{0.57}$ (e.g. Eker *et al.*, 2018), while the Einstein radius $\propto M^{0.5}$. Thus, $R \propto M^{0.07}$. The value of R remains fairly constant with increase in mass, and hence the point mass lens approximation holds true for even larger stars within typical galactic distances.

3. When all relevant distances are of order D , the Einstein Radius $\propto \sqrt{D}$, while the angular size of an object $\propto D^{-1}$, and hence $R \propto \frac{1}{\sqrt{D}}$. At large values of D ($> 1 \text{ kpc}$), the value of R is bound to decrease. However, for values of $D < 1 \text{ kpc}$, the value of R will begin to increase, and if D happens to be a few tens of parsecs, R will be of order unity. It is only in this unlikely scenario that the point mass approximation ceases to hold.

Given that the uniform sphere model is a highly simplified and unrealistic model, one may try to use an alternate mass distribution profile. One possibility is that of a polytrope of index $n = 3$, but as has been shown in Ohanian (1974), the difference is again noticeable only when R is of order unity.

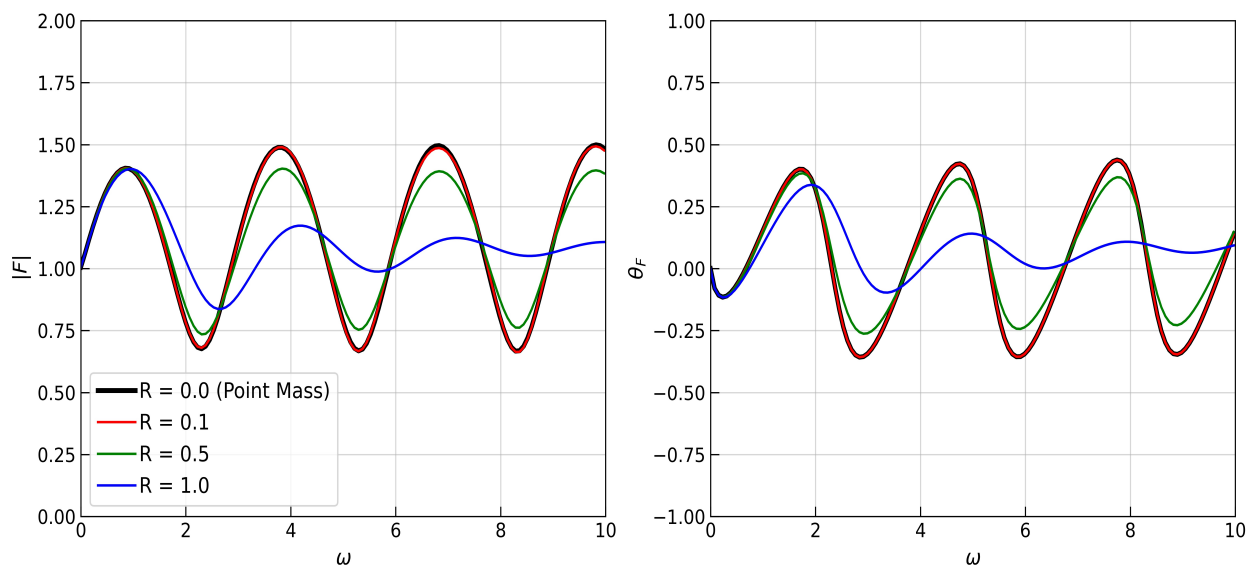


Figure 12. Comparison of uniform density sphere lenses to a point mass lens: absolute value and phase of the amplification factor as functions of dimensionless frequency, $\omega = 8\pi G(1 + z_d)M_L f/c^3$ are shown in left and right panel, respectively. The black line represents the point mass lens approximation. The colored lines represent the uniform density sphere approximation with different radii. When $R \sim 0.1$ (or smaller), the two models produce almost identical results. For $R > 0.4 - 0.5$, the point mass approximation is no longer valid.